CASE STUDY: PHASE COMPONENT AMPLITUDE VARIATION WITH ANGLE

Elita Selmara De Abreu[1], John Patrick Castagna[1], Gabriel Gil[2]

Right Running Head: Case study: PCAVA

[1]University of Houston, Department of Earth and Atmospheric Sciences, Houston, Texas, USA. E-mail: esdeabreu@uh.edu; jpcastagna@uh.edu.

[2]Lumina Technologies Inc., Research and Development, Houston, Texas, USA. E-mail: Gabriel.gil@luminageo.com.

ABSTRACT

In detectable and isolated thin layers below seismic resolution, phase decomposition can theoretically be used to discriminate relatively high-impedance thin-layer responses from low-impedance reservoir responses. Phase decomposition can be used to isolate seismic amplitudes with a particular phase response or to decompose the seismic trace into symmetrical and anti-symmetrical phase components. These components sum to form the original trace. Assuming zero-phase seismic data and normal American polarity, seismically thin layers that are high impedance relative to overlying and underlying half-spaces are seen on the +90^o phase component, while a relatively low-impedance thin layer will appear on the -90^o phase component. When such phase decomposition is applied to pre-stack attributes on a 2D line across a thin, 8-meter thick, gas-saturated reservoir in the Western Canadian Sedimentary Basin of Alberta, Canada, amplitude-variation-with-angle is magnified on the -90^o phase component. The -90^o far-offset component allows the lateral extent of the reservoir to be better delineated. This amplification is also seen on the -90^o phase component of the gradient attribute. These results are corroborated by seismic modeling which shows the same phase component relationships for near and far angle stacks as are observed on the real data. Fluid substitution and seismic modeling indicate that, relative to full-phase data, the mixed-phase response observed in this study exhibits variations in fluid effects that are magnified and better observed at far-angles on the -90^o phase component.

INTRODUCTION

The use of spectral decomposition applied to map lateral changes in acoustic properties and thickness of stratigraphic layers was first introduced to seismic interpretation by Partyka et

al. (1999). Since then, the use of spectral decomposition as an interpretational tool has been widely-accepted and applied to reservoir characterization (e.g., Matos et al., 2005, Liu and Marfurt, 2007), hydrocarbon detection (e.g., Castagna et al., 2003) and stratigraphic analysis (e.g., Hall and Trouillot, 2004).

In this paper, we assume that the seismic data have been "wavelet processed" for wavelet stability and that the wavelet phase has been corrected to zero phase using well control and synthetic seismograms (Roden and Sepulveda, 1999) or simple interface responses. Seismic phase is sensitive to subtle perturbations in the seismic signature, and phase attributes such as instantaneous phase can be used to detect lateral discontinuities and layer thickness variations (Taner, 1979). Assuming the wavelet and the impedance of a single layer within an analysis window is laterally stable, the phase response of a composite reflection will also be stable. However, in the presence of a lateral discontinuity such as a fault or a channel boundary, the phase will vary rapidly across that discontinuity (Partyka et al., 1999; Marfurt and Kirlin, 2001).

Most spectral decomposition techniques, such as the short-time Fourier Transform (STFT; Cohen, 1995), and the continuous wavelet transform, (CWT; e.g., Chakraborty and Okaya; 1995), produce complex spectra that can be represented by magnitude and phase components. However, spectral decomposition applications have been largely restricted to the magnitude component of the frequency spectrum, due to the difficulty of a straightforward interpretation of the phase spectra (Castagna et al., 2016; Matos et al., 2010).

Further complicating phase interpretation is the fact that the instantaneous phase and the phase spectrum are both independent of seismic amplitude envelope. Thus, when interpreting phase attribute variations for a composite reflection, one cannot independently directly ascertain the amplitude changes associated with given stratigraphic

symmetry components contributing to a seismic response. The seismic amplitude is related to the sum of all contributions, and, even in conjunction with phase cannot by itself reveal how an individual symmetry component is changing. For example, Castagna et al. (2016) show that slightly changing the symmetry of a closely-spaced even impulse pair may not change the overall amplitude or instantaneous phase of the composite reflection very much; but would greatly increase the magnitude of the asymmetrical phase component of that reflectivity pair.

Castagna et al. (2016) introduced a phase component approach (see methodology below) as a more interpretable way to understand the response phase of a seismic event, where the amplitude can be expressed as a function of both phase and frequency. As any waveform can be uniquely represented as the sum of symmetrical (even or zero-phase) and asymmetrical (odd or 90-degree phase) seismic responses (Bracewell, 1965), a composite reflection with mixed phase can be represented as the sum of odd and even phase components. We will present below a simple algorithm to determine these phase components. The application of phase decomposition on stacked data was shown to be a useful hydrocarbon indicator for seismically thin layers (Castagna et al.; 2016). This is related to the fact that changing the impedance in an isolated thin layer changes the phase of the local reflectivity by modifying the odd part of the reflectivity while the even part remains nearly unchanged. By decomposing the seismic response of such a composite reflection event into symmetrical and anti-symmetrical phase components that sum to form the seismic trace, amplitude variations due to changes of impedance within a thin layer manifesting in the odd component can be separated from background impedance effects contained in the even component that may obscure hydrocarbon-related amplitude anomalies. Furthermore, relatively

high-impedance isolated thin layers having positive phase can be separated from low-impedance layers having negative phase. Thus, amplitude variations due to hydrocarbons can be magnified on specific phase components and potentially distinguished from certain lithologic effects that also affect total amplitude. Assuming zero-phase seismic data and normal American polarity (i.e. an increase in impedance is seen as a positive peak on seismic data), gas-related amplitude variations in isolated seismically-thin low-impedance layers will show up best on the -90° phase component. Similarly, a high-impedance layer will appear in the +90° phase component.

The phase of the seismic data can be estimated by the correlating the seismic data with synthetics calculated from well logs. Initially, a statistical phase-zero wavelet is derived from the seismic data and used to generate synthetics at well locations. After improving the well-tie correlation through local shifts when necessary, we extract a well-log-based-wavelet where the phase is a free parameter to be adjusted to maximize the maximum correlation. If the seismic data is not zero phase, the phase of the wavelet should be considered in ascertaining the phase for which thin-layer effects will best be observed.

Other authors (Meza et al. 2016, Barbato et al., 2017) have shown the utility of phase decomposition for direct hydrocarbon detection. The objective of this paper is to study the application of phase decomposition to pre-stack seismic data. We apply phase decomposition to near- and far-angle stacks from a seismic line from the Western Canadian Sedimentary Basin of Alberta, Canada, through a well that encountered a shallow gas reservoir with 65% gas saturation. The amplitude-variation-with-angle (AVA) for 90° positive and negative phase components is compared to conventional AVA analysis. These observations are also compared to phase decomposition of pre-stack synthetics generated at the well and for fluid-substituted models.

METHODOLOGY

The phase decomposition used here is accomplished with the following procedure:

(1) The seismic trace, $d(t)$, is viewed as the real part of a complex analytic signal, $s(t)$, where the imaginary part is the Hilbert transform of the seismic trace, $H(d(t))$,

$$s(t) = d(t) + iH(d(t)). \quad (1)$$

The instantaneous phase, $\phi(t)$, is then given by

$$\phi(t) = \arctan\ (H(d(t))/d(t)). \quad (2)$$

and the instantaneous amplitude, $A(t)$ is

$$A(t) = \sqrt{(H(d(t))^2 + d(t)^2)}. \quad (3)$$

(2) All $A(t)$ maxima are identified and assigned an index, i, in the order in time for which each maximum occurs. Thus, the first maximum is assigned the index 1, the second maximum index = 2, and so on.

(3) At the time of each $A(t)$ maximum, t_i, a segment of the seismic trace, $d_i(t)$, is taken around t_i, from the preceding to the following $A(t)$ minimum.

(4) Each segment, $d_i(t)$, is divided into its unique even, $E_i(t)$, and odd, $O_i(t)$, parts (Bracewell; 1965) using:

$$E_i(t) = (d_i(t - t_i) + d_i(t + t_i))/2. \quad (4)$$

and

$$O_i(t) = (d_i(t - t_i) - d_i(t + t_i))/2. \quad (5)$$

where

$$d_i(t) = E_i(t) + O_i(t). \quad (6)$$

(5) Each even and odd segment is assigned a response phase, $\phi_i(t)$, which is the instantaneous phase of the segment at t_i. To first order, the response phase at an instantaneous amplitude peak is the instantaneous phase at the dominant frequency of a Fourier Transform of the signal windowed around the amplitude peak (Barnes, 1993). If care is taken in adequately sampling the data, the response phases will occur in the vicinity of -180^o, -90^o, 0^o, $+90^o$ and $+180^o$ for the even and odd parts If sampling is imperfect, some phase band around these values can be used to collect segments with approximately the same response phase.

(6) These phase components are produced by summing the segments exhibiting each response phase. Samples at $A(t)$ minima which are shared by two segments are averaged between the overlying and underlying segment.

The resulting phase component traces show the seismic amplitude associated with each phase. As they are defined by the response phase, the phase components will exhibit vertical striping related to the time duration of the segments. This striping is essential to the method. The output phase component stripe can be laterally smoothed or median filtered away for cosmetic purposes, but we choose not to do so as it could obscure the interpretation. Similarly, using time-variable instantaneous or spectral phase rather than constant response phase as a function of time for each segment would produce less trace-to-trace striping, but the interpretive meaning would be less clear.

To study the phase-component amplitude-variation-with angle (PCAVA) we start with angle stacks (near, mid, and far angles) for a seismic line distributed with the Hampson-Russell AVO software package (e.g., Russell et al., 2011). As shown in figure 1, phase decomposition is performed independently on each angle stack. We focus on three phase components provided by

phase decomposition: 0^o, -90^o, and $+90^o$. The amplitude-variation-with-angle analysis is applied to each individual phase component.

As discussed in Puryear and Castagna (2008), a simple thin layer with one reflection at the top and one at the base has a reflectivity that can be uniquely decomposed into even and odd impulse pairs. As also discussed in Castagna et al., (2016), for zero-phase seismic data and a composite seismic response from a simple thin layer, the 0° component is the response from that part of the reflectivity accounted for by equal positive reflection coefficients at top and base as would result from a stair-stepping increase in impedance with depth. Similarly, the 180° component would result from a stair-stepping decrease in impedance. Amplitudes for the +90° and -90° phase components will result from any asymmetry in the reflection coefficients from top and base. Variations in reflection coefficient symmetry can be due to variation of both lithological and fluid effects. Significantly, for an isolated thin layer and a zero-phase wavelet, the change in seismic response caused by the replacement of brine with hydrocarbons is always -90°. Thus, we expect variations in reflectivity due to hydrocarbons to be displayed in the asymmetrical (odd) phase components. If the reservoir rock is low impedance (causing a "bright spot"), the amplitude changes due to hydrocarbons will appear in the -90° phase component. In terms of AVO response (Rutherford and Williams, 1989), for Class III and Class IV sands (Castagna et al., 1998) the result would be a brightening of the -90^o angle stacks, particularly for far angles. For Class I gas sands the result would be a dimming on the $+90^o$ angle stacks, particularly at near angles. For Class II sands a variety of behaviors could occur, including possibly a dimming of $+90^o$ at near angles and brightening of -90^o at far angles. Using phase decomposition, the contribution to the seismic amplitude due to the even component of the reflectivity will be separated from this hydrocarbon effect. Thus, in the case of bright spots, the

fractional change in amplitude due to hydrocarbons in a thin layer can be most anomalous on the odd phase components. This should magnify hydrocarbon-related AVA effects for Class III (Rutherford and Williams, 1989) and bright Class II (Ross and Kinman, 1995) gas sands. Similarly, when gradients are negative for thin layers, they may also be enhanced on the -90° phase component by removing even component contribution to the AVA effects.

RESULTS

Colony Reservoir, Alberta – Canada

The Lower Cretaceous Colony Member fluvial channel sandstones in the Western Canadian Sedimentary Basin of Alberta, Canada can be prolific gas reservoirs. Seismic data has been effective in exploring for these reservoirs (Cederwall, 1989). The Colony Member consists of shales, siltstones, coals, and sandstones. The sandy portions are related to thick shoestring channels containing unconsolidated sandstones. These channels trend south to north and northwest throughout much of east-central Alberta and Saskatchewan (Putnam and Oliver, 1982). The channels are tens of kilometers in length and on the order of one kilometer wide. The Colony Member reservoir sandstones consist of multiple stacked paleo-channel deposits (Wightman et al., 1987). The hydrocarbon reservoirs occur at a depth of about 550 m, with thicknesses up to 10 m, although channels of 35-40 m have been observed (Cederwall, 1989). Well-log analysis indicates porosities as high as 30%, and permeability as high as several Darcys.

Figure 2 (from Cederwall, 1989) shows a geological cross-section of five wells (the inter-well distance is not to scale). The Colony Member channel facies is shown in the three central

well logs (10-10, 10-2 and 7-33). The channel is characterized by the gamma ray curve on the left as fining upward sandstones.

The data used for this study are CDP gathers from a 2D seismic line across a Colony member channel, distributed with Hampson-Russell software (Russell et al., 2011), along with one well containing sonic and density logs that can be used for seismic modeling. Figure 3 (bottom) shows the stacked seismic section with an amplitude anomaly on the picked blue horizon. A well at CDP 330 encountered 8 m of gas between 630 and 640 ms and a possible gas-water contact (or possibly a lowest known gas between channel members) that is seismically unresolved on the 2D line. Figure 3 (top) shows pre-stack gathers near the well location. The gas-filled channel sand exhibits an anomalous amplitude increase with offset. Gamma ray, resistivity, spontaneous potential, sonic, and density logs were provided with the well data. We used the Greenberg-Castagna (1992) method to estimate shear-wave velocity. The well logs and seismic tie are shown in Figure 4. Figure 5 shows that the gas-sand has an anomalously low ratio of compressional-to-shear-wave velocities (V_p/V_s).

The average P-wave velocity at the gas zone is 2400 m/s. The gas interval (633 to 640.6 meters - TVD) is known to be about 8 meters thick (about 7 ms at the well location), which means that we would need a wavelet of about 75 Hz peak frequency to be able to resolve it (if it were a simple isolated thin layer). However, the peak frequency of the real data wavelet at the reservoir interval is 35 Hz (figure 6). Following Widess (1973), this wavelet frequency implies a time resolution of about 14 ms corresponding to a half-period (or about a 17 m tuning thickness corresponding to ¼ wavelength) for an isolated layer. According to Wightman et al. (1987), reservoir thickness below 6 m is very common in this area.

A wedge model using the well-log elastic properties (density, P-wave velocity, and calculated S-wave velocity) at the gas reservoir is shown in figure 7. The left-hand side of the plot shows the P-wave velocity model, and the right-hand side shows the synthetic using a 35 Hz Ricker wavelet. The top of the gas zone (633 m) was fixed and the base varied from 0 to 100 meters below with an increment of 4 meters. The layer properties below the base were shifted vertically as the thickness varies. The time thickness measured from the seismic data as well as in the wedge model (peak-to-trough) at the well location is 12 ms, which is reasonable given that the peak-trough time becomes insensitive to thickness below tuning.

There are also complications due to the interference of many reflectors. In figure 4, it is evident that the reservoir is not a single homogeneous layer nor is it isolated from other reflections above and below. According to Widess (1973), the tuning thickness is about ¼ λ for a zero-phase Ricker wavelet for a high or low-impedance layer encased in a constant impedance background above and below, i.e., a pair of odd reflection coefficients with the same absolute value. Since this does not apply in our case, the background above and below the reservoir is different and the reservoir is not homogeneous, the synthetic tuning curve will deviate from the Widess prediction.

Amplitude-versus-angle (AVA) analysis

The AVA analysis is based on the Shuey (1985) approximation of the Zoeppritz equation, where the reflectivity is described as a function of the angle $r(\theta)$ which varies according to the following equation:

$$r(\theta) \approx A + Bsin^2\theta + Csin^2\theta tan^2\theta + ... \quad (7)$$

where A is the intercept, which is equivalent to the reflectivity at $\theta = 0^o$ and is given by

$$A = \frac{1}{2}\left(\frac{\Delta v_p}{v_p} + \frac{\Delta \rho}{\rho}\right) \cong r(0^o). \quad (8)$$

B is the gradient or slope;

$$B = A - k\left(\frac{\Delta v_s}{v_s} + \left(\frac{1+k}{2k}\right)\frac{\Delta \rho}{\rho}\right). \quad (9)$$

where $k = 4\left(\frac{v_s}{v_p}\right)^2$ and C is the curvature, given by

$$C = \frac{1\Delta v_p}{2\ v_p}. \quad (10)$$

For small angles ($< 30^0$), the C term and higher orders can be neglected and the equation (7) becomes the well-known two-term Shuey (1985) equation:

$$r(\theta) = A + Bsin^2\theta. \quad (11)$$

A primaries-only synthetic seismogram using the well logs and the statistical wavelet extracted for the interval (figure 6) was calculated for incidence angles from 0° to 30° and the synthetic AVA response was compared to the seismic angle gather at the well position (figure 8). The amplitude variations at the top of the gas reservoir for the synthetic seismogram and angle gathers are similar and the amplitude behavior with angle confirms the bright spot seen on the stacked section. The amplitude at the top of the reservoir is negative at small angles and becomes more negative with increasing angle to 30°. As the seismic gathers are not amplitude calibrated to the well, the real and synthetic amplitudes do not match each other (Lin and Thomsen, 2013). The synthetic has amplitudes about 2.5 times stronger than the real data, but the synthetic and

real data amplitudes vary similarly with the absolute value of amplitude (magnitude) increasing with increasing angle.

To demonstrate that this behavior could be a fluid effect, a fluid substitution from gas to brine using Gassmann's equation and the in situ well log properties was performed in the reservoir and a synthetic seismogram was also calculated and compared to the seismic angle gather. As we can see in figure 8, the amplitude at the top of the brine-filled reservoir rock at near angles (0^o to 5^o) is positive. As the angle increase, the amplitude at the top of the brine-filled reservoir rock decreases. In the gas-case, the absolute value of amplitude (magnitude) increases with angle.

The anomaly can also be identified and analyzed by computing AVO attributes directly from the gathers. The following attributes were generated: the 0^o-10^o near angle stack, the 10^o-20^o mid angle stack, the 20^o-30^o far angle stack, the AVO intercept, the AVO gradient, the intercept times gradient product, and the scaled Poisson's ratio (figure 9). Both intercept and gradient are negative for the top of reservoir reflection (figure 9-b). This behavior is highlighted by the product attribute (figure 9-c) where both top and base of the reservoir exhibit a distinct positive response. The scaled Poisson's ratio attribute (e.g., Verm and Hilterman, 1995) indicates a transition from high to low Poisson's ratio values at the top of the reservoir which could be indicative of gas (figure 9-d). Note that the scaling was such that the scaled Poisson's ratio is the average of the AVO intercept and AVO gradient and is designed for the target level only, resulting in false anomalies in the deeper section.

Phase decomposition analysis

As has been demonstrated by Castagna et al. (2016), Meza et al. (2016), and Barbato et al. (2017), if we assume a zero-phase wavelet there are specific phase components that can be analyzed to enhance anomalous behavior. The 0^o phase component may indicate isolated interfaces with an increase in impedance such as water-contacts, or a sub-tuning thin interval with primarily positive reflection coefficients. The $+90^o$ phase component may indicate thin relatively high-impedance layers or a long transitional increase in impedance. Relatively low-impedance thin layers, that could be due to hydrocarbons, porosity increases, or other lithological variations, show up on the -90^o component. A zero-phase wavelet produced an imperfect seismic tie judged to be adequate since the correlation of the synthetic with the gathers is above 0.80 (figure 6). We, therefore, assumed the data were zero phase and performed phase decomposition (Castagna et al., 2016) on the stacked gather outputting the 0^o, $+90^o$, and -90^o phase components (figure 10).

The comparison of the seismic stack with the phase components (figure 10) shows good agreement with our understanding of the geology of the area. As described earlier, the Colony member is a complex of stacked channels. Its total thickness varies ~~vary~~ from very thin layers up to 10 meters. Gas discoveries have been associated with bright spot anomalies on the seismic data (Wightman et al., 1987) although bright spots alone are not definitive indicators of gas here due to lithological and tuning variations. Thus, the need for AVO analysis and enhancing that analysis with phase decomposition. The presence of high-impedance carbonates may occur in between the channel sands due to either a sea level increase (depending on the position) or to differing cementation. In our case study, it is possible to see the presence of these carbonates right below the gas reservoir where we have an increase of well-log resistivity, density, and P-

wave velocity, while the gamma-ray log indicates low shale content, suggesting clean carbonates (figure 4).

Note that in Figure 10, the channel sand appears to be a structural high on the stacked section, though events above and below are flat. Phase decomposition, however, reveals that the channels sand is strongest on the -90^o phase component (figure 10-d) while the apparent "off structure" events are strongest on the $+90^o$ components, indicating a polarity reversal at the top of the gas sand, creating a false structure. By flipping the formation top pick on the stack from a peak "off structure" to a trough at the top of the reservoir, the structure becomes flatter as are the overlying and underlying events. This is most apparent on the phase decomposition of the far offset stack discussed in the next section.

The $+90^o$ phase component in figure 10-b highlights a presumable carbonate high-impedance thin layer just below the reservoir to the right of the well. It also shows distinct dimming at the reservoir level at and around the well.

The -90^o phase component (figure 10-d) has good agreement with the observable bright spot on the seismic data at the well (figure 10-a) as expected. It also delineates the extension of the gas-saturated reservoir to the left side of the well position. The vertical striping is a consequence of the phase decomposition algorithm employed that is based on the response phase and thus segments the trace between instantaneous amplitude minima, giving constant response phase over discrete time intervals. This is the nature of response phase attributes which are blocky rather than smooth.

Another hard interface is seen in the 0^o phase component around 690 ms (figure 10-c), which corresponds to the Pre-Cretaceous unconformity (Cederwall, 1989).

We note that interpretation of the phase components on the stack is somewhat complicated by interference with interpreted laterally changing geology just below the reservoir. It remains to be seen below if this ambiguity can be resolved prestack by accentuating hydrocarbon effects relative to lithological ones.

Phase-component-amplitude-versus-angle (PCAVA) analysis

We applied phase decomposition to the near (0^o-10^o) and far (20^o-30^o) angle stacks and analyzed how the phase component amplitudes vary with the angle (PCAVA) (figure 11).

The amplitude difference between near and far angle stack at the top of the reservoir (figure 11, a and e respectively) is reinforced by the -90^o phase components (figure 11, c and g respectively), showing a stronger PCAVA effect due to the presence of gas than the original data. As we can see in figure 11-g, the -90^o far component shows a more laterally extended bright spot around the well than is evident on the seismic stacked data (figure 10-a) or its -90^o phase component (figure 10-d). At the well location, there is a good correlation between real and synthetic phase components (see inserted curves in figures 10 and 11).

Phase decomposition was also applied to in situ and fluid-substituted synthetics to verify the hydrocarbon effect (figure 12) on the phase components. For the brine case, no amplitude-variation-with-angle could be observed on the -90^o phase component. However, for the gas case, the main contribution to the amplitude-variation-with-angle comes from the -90^o phase component at angles above 20^o (corresponding to far stack angles).

These synthetic and real data results suggest that PCAVA can aid in the detection of hydrocarbons in seismically thin layers and better delineate the reservoir extension.

The AVA gradient, *B*, from the Shuey (1985) two-term approximation (equation (11)), also known as the slope attribute, shows how the amplitude varies with angle. The gradient attribute is a commonly used hydrocarbon indicator, since it is a combination of contrasts in compressional-wave velocity, shear-wave velocity, and density, and the background ratio of compressional-to-shear-wave velocities (see equation (9)) and is directly related to anomalous velocity ratios. For a class III AVO response, we expect a negative gradient at the top of the reservoir and a positive one at the base. As we can see in figure13-a, the gradient is very negative at the top of the reservoir, where the velocity ratio calculated from the well logs gets very low relative to the background, and it becomes very positive at the base of the reservoir, where the velocity ratio increases again.

Figure 13 shows the result of phase decomposition on the gradient section. The reservoir is particularly anomalous on the -90^{o} phase component of the gradient and ties the phase decomposition of the synthetic at the target (figure 13-d). However, there is anomalous behavior above and below the reservoir that does not tie the synthetic. Inspection of the gathers at these locations (Figure 14) shows a loss of data quality and residual NMO at the far offsets for these events, resulting in erroneously extracted gradients. The gradient attribute itself is known to be noisier than partial stacks (Swan, 1993), and the phase decomposition has amplified that noise, in addition to the anomalous behavior (figure 15). We conclude that phase decomposition must be used with caution when applied to noisy seismic data or attributes.

CONCLUSIONS

Phase decomposition provides a new way of interpreting seismic data. Thin beds, subtle fluid responses and changes in lithology, otherwise hidden in seismic waveforms, can be

potentially amplified on specific phase components. In this study we applied phase decomposition to pre-stack data on a 2D line across a gas-bearing channel in Canada and found the following:

(1) the strength and lateral extent of a gas-related AVA anomaly is increased on the -90^o phase component;

(2) there are good ties between phase components on real and synthetic near- and far-angle stacks;

(3) an interpreted high-impedance response is obvious on the +90^o phase component to the right of the well, presumably due to increased carbonate thickness;

(4) phase decomposition of the gradient attribute shows anomalous behavior at the reservoir that ties the synthetic result, but also is sensitive to noise above and below the target, where there is a poor match between real and synthetic data.

These results are corroborated by phase decomposition of fluid-substituted synthetic gathers. The comparison between the brine-saturated and the gas-saturated synthetics shows that on the -90^o phase component no amplitude variation is observed for the brine-case, while for the gas-case, most of the contribution to the amplitude-variation-with-angle comes from the angles above 20^o for this same component.

Although the process of phase decomposition doesn't require well information, calculation of synthetics and correlation with observed responses on seismic data helps in understanding phase component responses and in building confidence in their use in direct hydrocarbon indication.

ACKNOWLEDGMENTS

We would like to thank CGG for use of the data and use of the Hampson-Russell AVO software package at the University of Houston. Thanks to Firas Al-Jarrah and Azie Aziz, formerly with Lumina Technologies, for their assistance.

REFERENCES

Barbato, U., O. Portniaguine, B. Winkelman, and J. Castagna, 2017, Phase decomposition as a DHI in bright-spot regimes: A Gulf of Mexico case study, SEG Technical Program Expanded Abstracts 2017: pp. 3976-3980, doi: https: 10.1190/segam2017-17737608.1.

Barnes, A. E., 1993, Instantaneous spectral bandwidth and dominant frequency with applications to seismic reflection data, Geophysics, **58**, 419-428.

Castagna, J. P., Swan, H. W., and Foster, D. J., 1998. Framework for AVO gradient and intercept interpretation: Geophysics, **63**, p. 948-956.

Castagna, J., A. Oyem, O. Portniaguine, and U. Aikulola, 2016, Phase decomposition. Interpretation, **4**, no. 3, SN1-SN10, doi: 10.1190/INT-2015-0150.1.

Cederwall, Dale A., 1989, The Lower Cretaceous, *in* N. L. Anderson, L. V. Hills, and D. A. Cederwall, eds., The CSEG/CSPG geophysical atlas of Western Canadian hydrocarbon pools. Chapter 8, pp. 260-266.

Dvorkin, J, and Nur, A., 1996, Elasticity of high-porosity sandstones: Theory for two North Sea data sets: Geophysics, **61**, 1363-1370.

Lin, R. and L. Thomsen, 2013. Extracting Polar Anisotropy Parameters From Seismic Data And Well Logs, Soc. Expl. Geoph. Annl. Mtg. Expnd. Absts., 83, 310-314.

Marfurt, K. J., and R. L. Kirlin, 2001, Narrow-band spectral analysis and thin-bed tuning: Geophysics, **66**, p. 1274-1283.

Meza, R., G. Haughey, J. Castagna, U. Barbato, and O. Portniaguine, 2016, Phase decomposition as a hydrocarbon indicator: A case study, SEG Technical Program Expanded Abstracts, pp. 1839-1843, doi: 10.1190/segam2016-13871199.1.

Ødegaard, E. and Avseth, P., 2003, Interpretation of elastic inversion results using rock physics templates: EAGE, Expanded Abstracts.

Puryear, C., and J. P. Castagna, 2008, Layer-thickness determination and stratigraphic interpretation using spectral inversion: Theory and application: Geophysics, **73**, R37-R48.

Putnam, P.E. and T. A. Oliver, 1980, Stratigraphic traps in channel sandstones in the Upper Mannville (Albian) of east-central Alberta: Bulletin of Canadian Petroleum Geology, **28**, p. 489-508.

Ross, C. P. and D. L. Kinman, 1995, Nonbright-spot AVO: Two examples, Geophysics, **60**, no.5, 1398-1408. doi: 10.1190/1.1443875.

Russell, B., D. Gray, and D. Hampson, 2011, Linearized AVO and poroelasticity: Geophysics, **76**, no. 3, C19– C29, doi: 10.1190/1.3555082.

Rutherford, S. R., and R. H. Williams, 1989, Amplitude-versus-offset variations in gas sands: Geophysics, **54**, 680–688.

Shuey, R. T., 1985. A simplication of Zoeppritz equations. Geophysics, **50**, p. 609-614.

Swan, H. W., 1993, Properties of direct AVO hydrocarbon indicators, *in* J. P. Castagna and M. M. Backus, eds., Offset-dependent Reflectivity—Theory and practice of AVO analysis: Soc. Expl. Geophysics, 78–92.

Taner, M. T., Koehler, F., e Sheri, R. E., 1979. Complex seismic trace analysis. Geophysics, **44**, p. 1041-1063.

Verm, R. and Hilterman, F., 1995, Lithology color-coded seismic sections: The calibration of AVO crossplotting to rock properties: The Leading Edge, **14**, no. 08, 847-853.

Widess, M., 1973, How thin is a thin bed?: Geophysics, **38**, 1176-1180.

Wightman, D. M., S. G. Pemberton and G. Singh, 1987, Depositional modeling of the Upper Mannville (Lower Cretaceous), Central Alberta: Implications for the recognition of brackish water deposits, *in* R. W. Tillman and K.J. Weber, eds., Reservoir Sedimentology: Soc. Econ. Paleontol. Mineral, Spec. Publ., **40**, pp. 189-220.

LIST OF FIGURES

Figure 2: Geological cross-section from Cederwell (1989) of the Hairy Hills Colony W pool, highlighting the Colony sand channel development. The logs in each well are gamma ray (leftmost) and spontaneous potential (rightmost). Note that the horizontal distance in between the wells is given in kilometers, while the vertical distance along the wells is given in meters.

Figure 3: 2D line showing the well location (CDP 330) at the gathers (top) and at the stacked gathers (bottom). The well (red) is represented by the P-wave velocity curve and the top of the reservoir is represented by the blue horizon. Note that the minimum offset is 50 meters and maximum is 650 meters.

Figure 4: Well log section at the reservoir zone. Measured curves are shown in black, calculated curves are shown in red. The right panel shows the P-impedance (red curve) correlation with the full stack seismic data. There may be a slight flattening on the seismic data due to a possible water-contact at base gas, but the resolution is not sufficient to interpret this unambiguously. However, note that this event coincides with a thin high impedance layer indicating a lithologic change that could separate different sand members in the channel. This means there could be an associated permeability barrier between channel sands here (as noted occurs in the Colony channels by Wightman; 1987). That the base-gas event follows structure suggests that it could be a lowest-known-gas response. The time thickness of the reservoir at the well is slightly below ½ period which is the tuning time thickness. Thus, any water-contact event would be at or below seismic resolution.

Figure 5: Crossplot of P-Impedance and the ratio of compressional-to-shear-wave velocities (Vp/Vs) calculated from the well logs. The gas reservoir is highlighted by the red circle. The rock physics template (RTP) curves plotted are available on the Hampson-Russel, a

CGG's software and were calibrated to shale (top curve), and clean sandstone for different saturations (bottom curves). The RTP method is based on theory proposed by Dvorkin and Nur (1996) and Ødegaard and Avseth (2003).

Figure 6: Well tie section. (a)Well logs (b) Synthetic tie to extracted trace (c) Seismic section with extracted trace highlighted in red (d) Correlation of synthetic versus seismic versus time shift (e) Extracted wavelet and (f) Extracted wavelet spectrum. The maximum correlation obtained for a zero-phase statistical wavelet extracted from seismic was 0.853. There appear to be slight timing discrepancies between synthetic and real data, but no stretching or squeezing was applied to preserve the integrity of the data. The hard streak at 660 ms shows a peak-over-through response on the synthetic (blue wiggle trace) but is absent on the extracted seismic trace (red wiggle trace). This could mean the tight interval is highly localized at the well or obscured by noise. The missing peak does appear on the seismic section about 4 traces to the right. The correlation curve suggests that a phase shift of about 30 degrees may be required. This was not applied due to the uncertain well tie.

Figure 7: Wedge model generated by extrapolation of the well log elastic properties (density, P-wave velocity, and S-wave velocity) properties and a 35 Hz Ricker wavelet. At the left side we have the wedge model superposed with the extrapolated P-wave velocity from the well log while at the right side we have the wedge model superposed with the seismic amplitude. Note that the P-impedance log is displayed at the corresponding well thickness. At the bottom we have the tuning curve (amplitude measured at the top of the reservoir (trough) versus thickness).

Figure 8: (a) real seismic gather (b) synthetic gather under in situ conditions (65% gas saturated) (c) fluid substituted 100% water saturated gather (d) comparison of the amplitude

variation with offset at the top of the gas-bearing interval from the synthetic and real gathers (e) comparison of the intercept versus gradient highlighting the top of the gas interval of synthetic brine (yellow), synthetic in situ (blue) and real gathers at the well location (red).

Figure 9: AVA attributes calculated for the seismic gather data with the P-wave synthetic seismogram calculated from the well logs inserted at the well position. a) stacked seismic data, b) intercept: A (wiggle) superposed on gradient: B (in color), c) intercept times gradient product: A*B, d) Scaled Poisson's ratio: aA+bB (a=0.5 and b=0.5).

Figure 10: Phase components of the seismic stack data with the phase decomposed synthetic trace from the well for the corresponding phase component displayed in the vertical section at the well position. a) stacked seismic data, b) +90° component, c) 0° component, d) -90° component.

Figure 11: Phase components of near (0°-10°) and far (20°-30°) angle stacks and the phase decomposed synthetic near and far trace from the well for the corresponding phase component displayed in the vertical section as wiggle traces at the well location. a) near angle stack with inserted Poisson's ratio curve, b) near stack +90° phase component, c) near stack 0° phase component, d) near stack -90° phase component, e) far angle stack with inserted Poisson's ratio curve, f) far stack +90° phase component, g) far stack 0° phase component, h) far stack -90° phase component.

Figure 12: Phase components for fluid-substituted pre-stack synthetics calculated from the well logs. The two panels in the left (yellow highlighted) show the synthetic data for the gas and brine saturated cases. The following 4 panels in the center (red highlighted) show the phase components for the gas saturated case; and the last 4 panels in the right (blue highlighted) show

the phase components for the brine saturated case. The phase components displayed are labeled at the top of each track.

Figure 13: Phase component of the gradient calculated from seismic data. a): gradient with the Poisson's ratio log calculated from the well logs inserted at the well position,b) +90° component, c) 0° component, d) -90° component. The inserted trace for each panel is the phase decomposed synthetic trace from the well for the corresponding phase component displayed in the vertical section at the well position.

Figure 14: Original gathers at the well location (CDP 330) displaying the P-impedance (red curve) and resistivity (red curve) logs.

Figure 15: Comparison between the original gathers at the well location and the -90º phase component from the gradient attribute. The yellow arrows point to the loss of data quality at the far offsets for these events, resulting in anomalous -90° phase component from gradient.

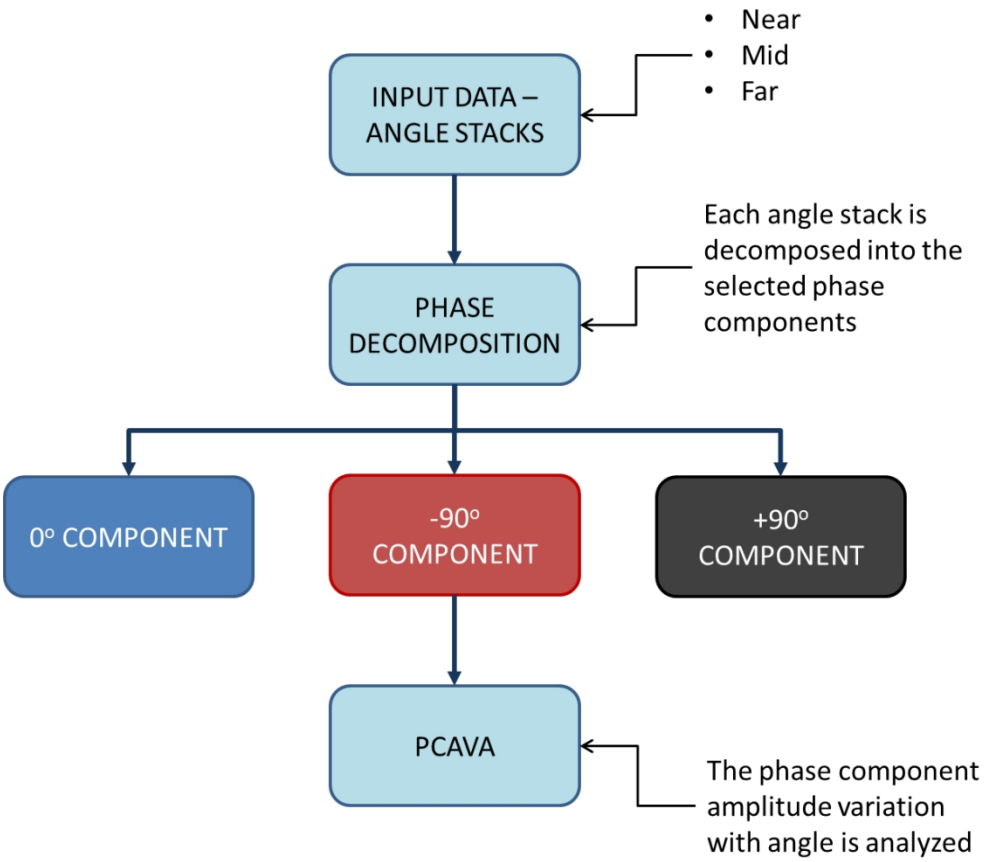

Figure 1: Workflow procedure applied to the PCAVA analysis.

106x94mm (300 x 300 DPI)

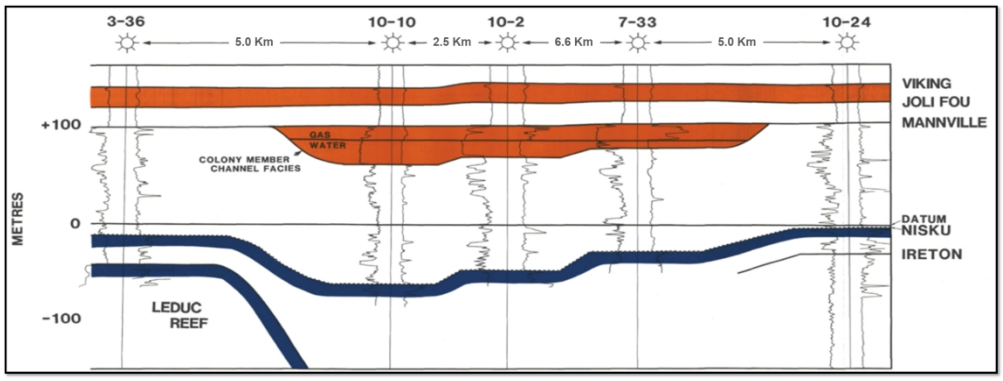

Figure 2: Geological cross-section from Cederwell (1989) of the Hairy Hills Colony W pool, highlighting the Colony sand channel development. The logs in each well are gamma ray (leftmost) and spontaneous potential (rightmost). Note that the horizontal distance in between the wells is given in kilometers, while the vertical distance along the wells is given in meters.

208x78mm (300 x 300 DPI)

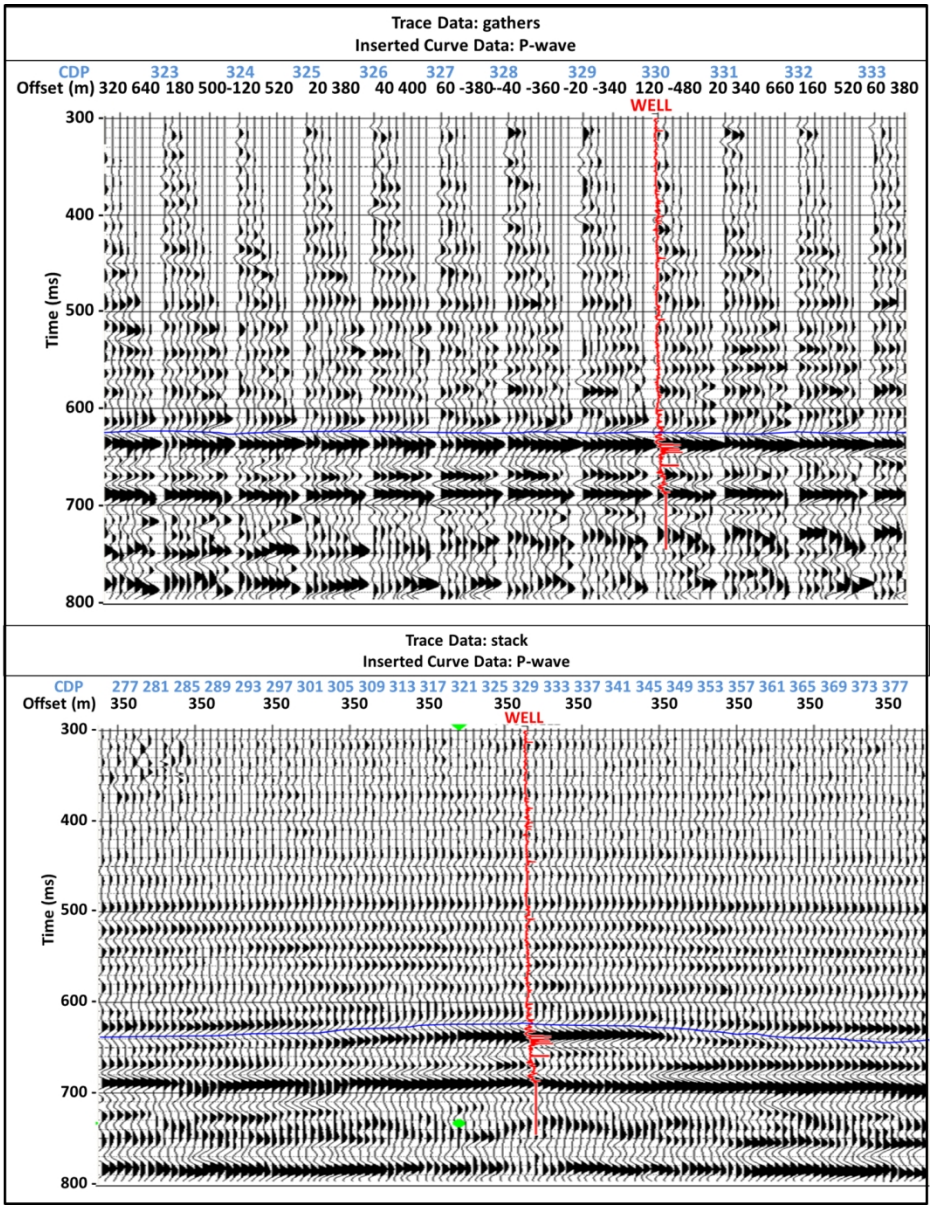

Figure 3: 2D line showing the well location (CDP 330) at the gathers (top) and at the stacked gathers (bottom). The well (red) is represented by the P-wave velocity curve and the top of the reservoir is represented by the blue horizon. Note that the minimum offset is 50 meters and maximum is 650 meters.

127x161mm (300 x 300 DPI)

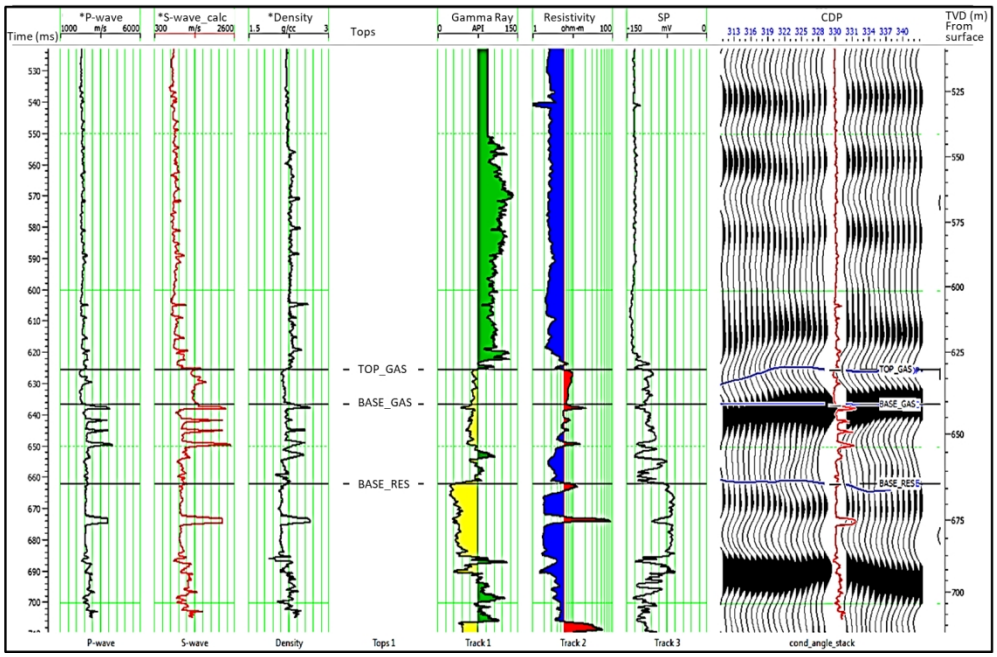

Figure 4: Well log section at the reservoir zone. Measured curves are shown in black, calculated curves are shown in red. The right panel shows the P-impedance (red curve) correlation with the full stack seismic data. There may be a slight flattening on the seismic data due to a possible water-contact at base gas, but the resolution is not sufficient to interpret this unambiguously. However, note that this event coincides with a thin high impedance layer indicating a lithologic change that could separate different sand members in the channel. This means there could be an associated permeability barrier between channel sands here (as noted occurs in the Colony channels by Wightman; 1987). That the base-gas event follows structure suggests that it could be a lowest-known-gas response. The time thickness of the reservoir at the well is slightly below ½ period which is the tuning time thickness. Thus, any water-contact event would be at or below seismic resolution.

147x95mm (300 x 300 DPI)

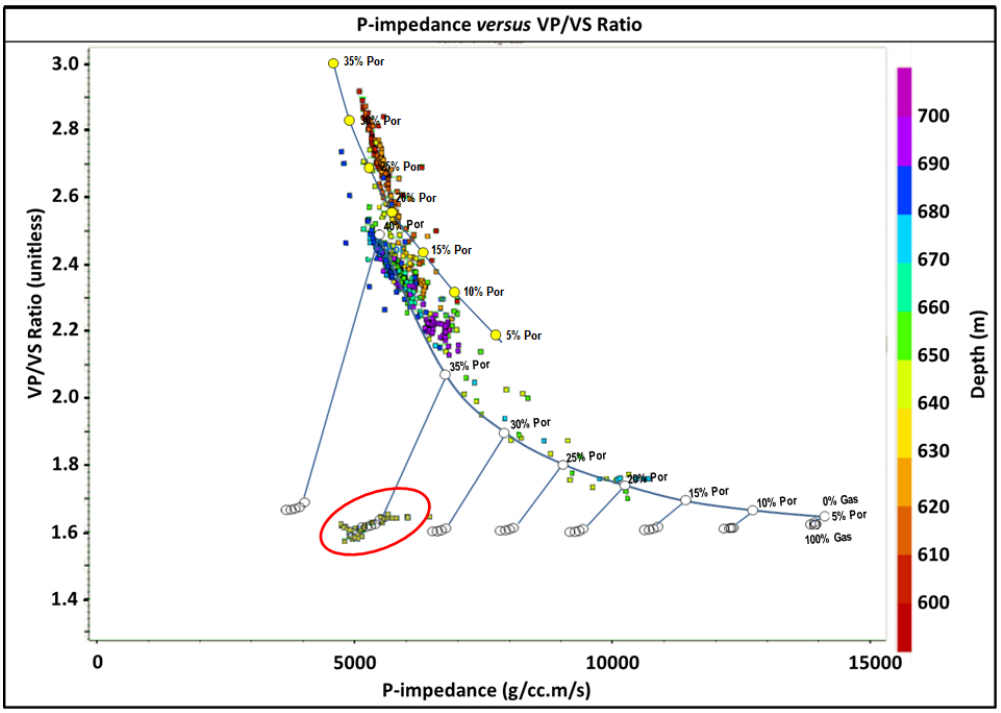

Figure 5: Crossplot of P-Impedance and the ratio of compressional-to-shear-wave velocities (Vp/Vs) calculated from the well logs. The gas reservoir is highlighted by the red circle. The rock physics template (RTP) curves plotted are available on the Hampson-Russel, a CGG's software and were calibrated to shale (top curve), and clean sandstone for different saturations (bottom curves). The RTP method is based on theory proposed by Dvorkin and Nur (1996) and Ødegaard and Avseth (2003).

81x57mm (300 x 300 DPI)

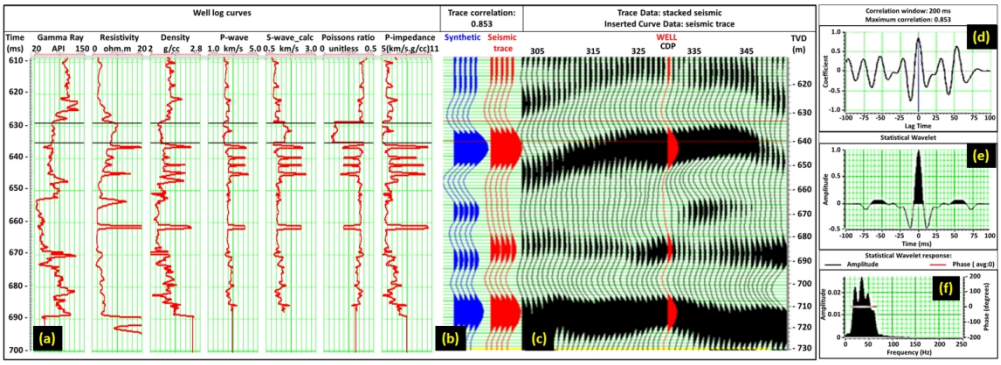

Figure 6: Well tie section. (a)Well logs (b) Synthetic tie to extracted trace (c) Seismic section with extracted trace highlighted in red (d) Correlation of synthetic versus seismic versus time shift (e) Extracted wavelet and (f) Extracted wavelet spectrum. The maximum correlation obtained for a zero-phase statistical wavelet extracted from seismic was 0.853. There appear to be slight timing discrepancies between synthetic and real data, but no stretching or squeezing was applied to preserve the integrity of the data. The hard streak at 660 ms shows a peak-over-through response on the synthetic (blue wiggle trace) but is absent on the extracted seismic trace (red wiggle trace). This could mean the tight interval is highly localized at the well or obscured by noise. The missing peak does appear on the seismic section about 4 traces to the right. The correlation curve suggests that a phase shift of about 30 degrees may be required. This was not applied due to the uncertain well tie.

133x47mm (300 x 300 DPI)

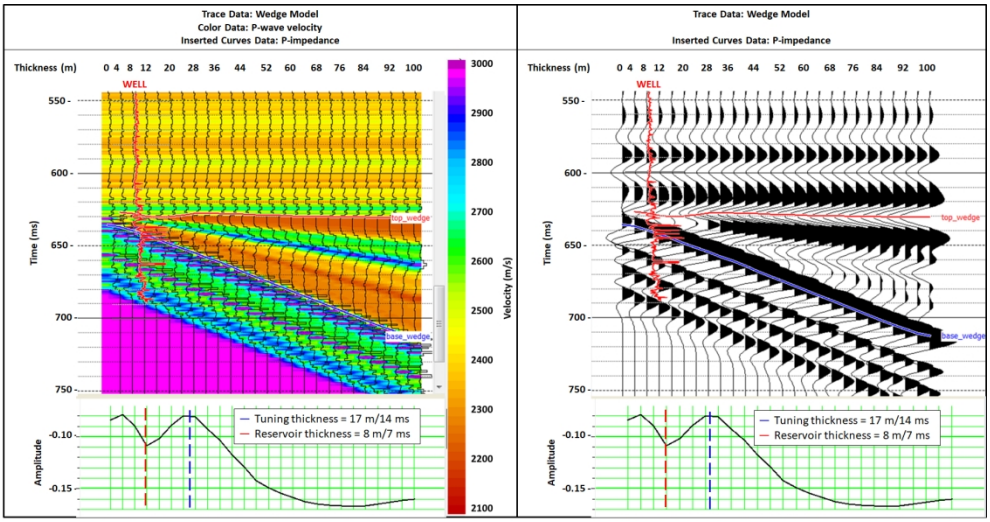

Figure 7: Wedge model generated by extrapolation of the well log elastic properties (density, P-wave velocity, and S-wave velocity) properties and a 35 Hz Ricker wavelet. At the left side we have the wedge model superposed with the extrapolated P-wave velocity from the well log while at the right side we have the wedge model superposed with the seismic amplitude. Note that the P-impedance log is displayed at the corresponding well thickness. At the bottom we have the tuning curve (amplitude measured at the top of the reservoir (trough) versus thickness).

164x84mm (300 x 300 DPI)

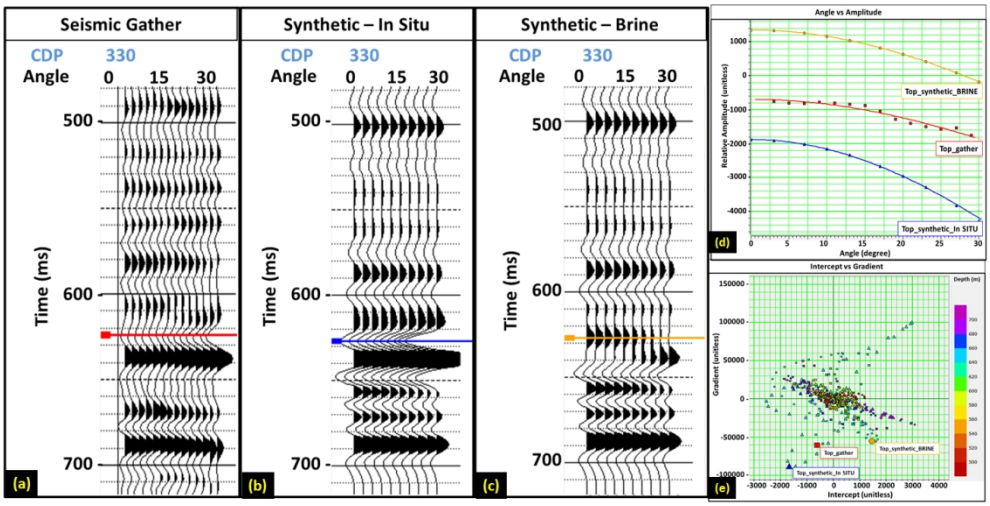

Figure 8: (a) real seismic gather (b) synthetic gather under in situ conditions (65% gas saturated) (c) fluid substituted 100% water saturated gather (d) comparison of the amplitude variation with offset at the top of the gas-bearing interval from the synthetic and real gathers (e) comparison of the intercept versus gradient highlighting the top of the gas interval of synthetic brine (yellow), synthetic in situ (blue) and real gathers at the well location (red).

123x61mm (300 x 300 DPI)

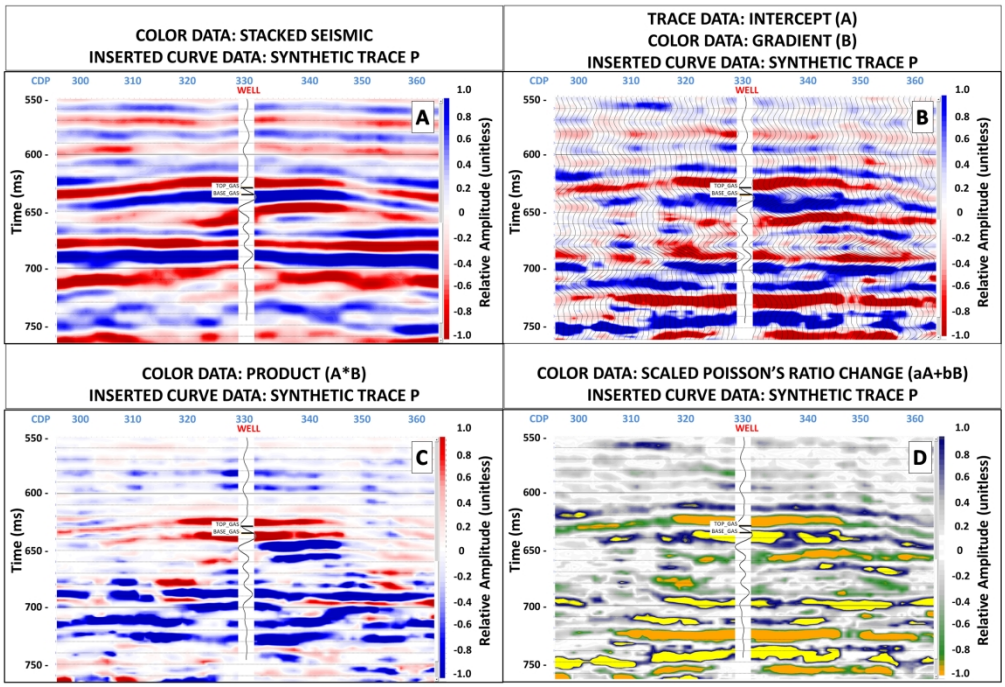

Figure 9: AVA attributes calculated for the seismic gather data with the P-wave synthetic seismogram calculated from the well logs inserted at the well position. a) stacked seismic data, b) intercept: A (wiggle) superposed on gradient: B (in color), c) intercept times gradient product: A*B, d) Scaled Poisson's ratio: aA+bB (a=0.5 and b=0.5).

198x135mm (300 x 300 DPI)

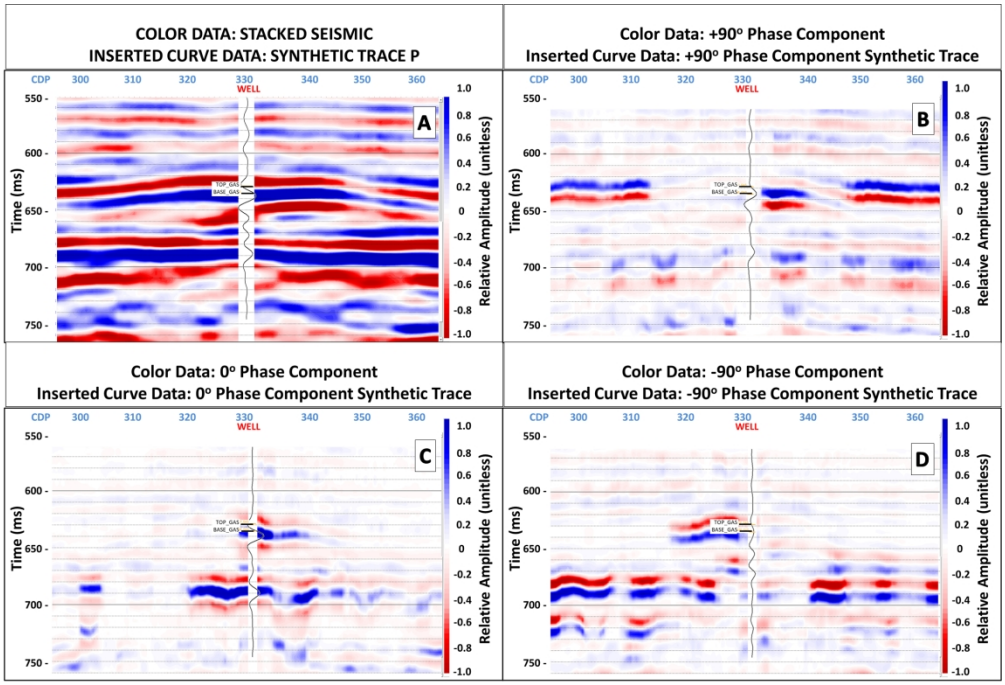

Figure 10: Phase components of the seismic stack data with the phase decomposed synthetic trace from the well for the corresponding phase component displayed in the vertical section at the well position. a) stacked seismic data, b) +90° component, c) 0° component, d) -90° component.

198x135mm (300 x 300 DPI)

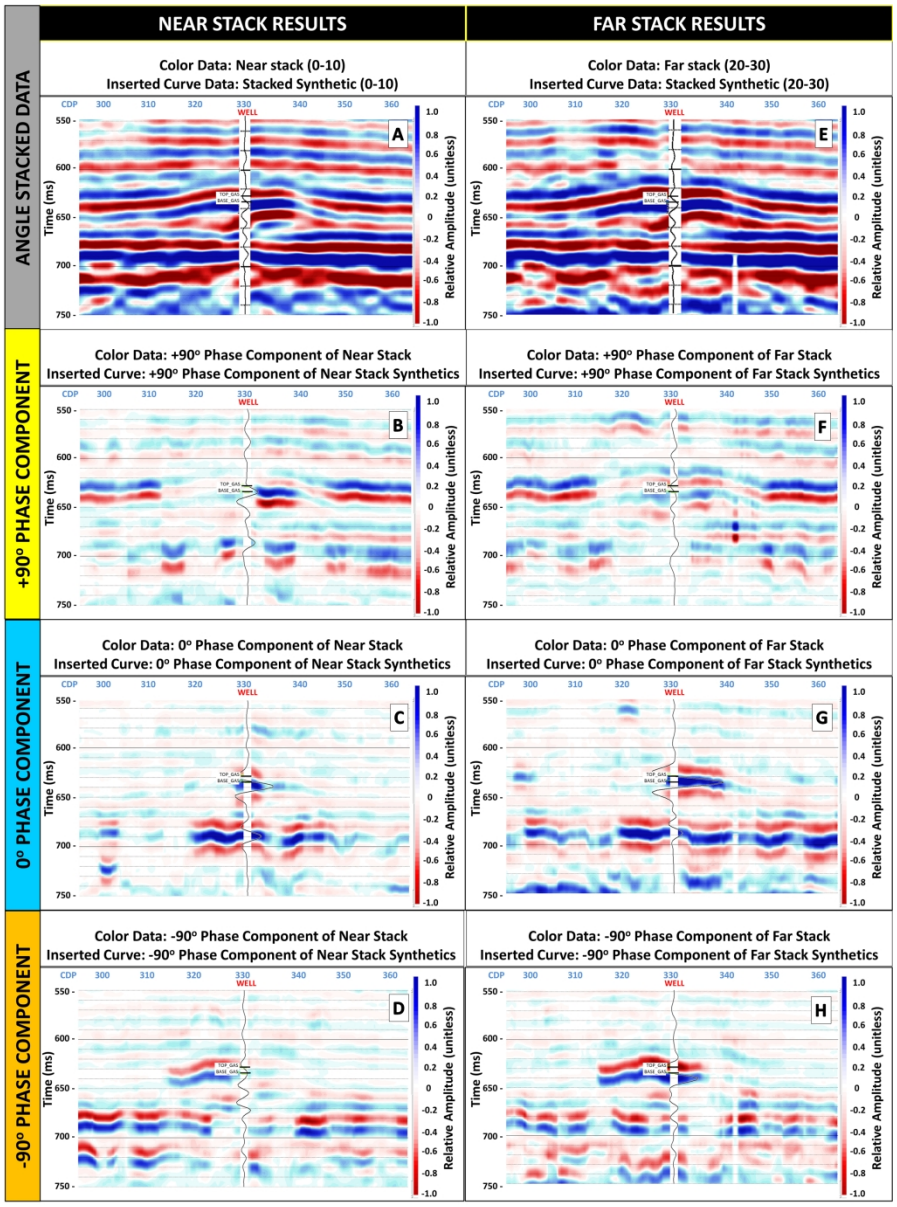

Figure 11: Phase components of near (0°-10°) and far (20°-30°) angle stacks and the phase decomposed synthetic near and far trace from the well for the corresponding phase component displayed in the vertical section as wiggle traces at the well location. a) near angle stack with inserted Poisson's ratio curve, b) near stack +90° phase component, c) near stack 0° phase component, d) near stack -90° phase component, e) far angle stack with inserted Poisson's ratio curve, f) far stack +90° phase component, g) far stack 0° phase component, h) far stack -90° phase component.

206x277mm (300 x 300 DPI)

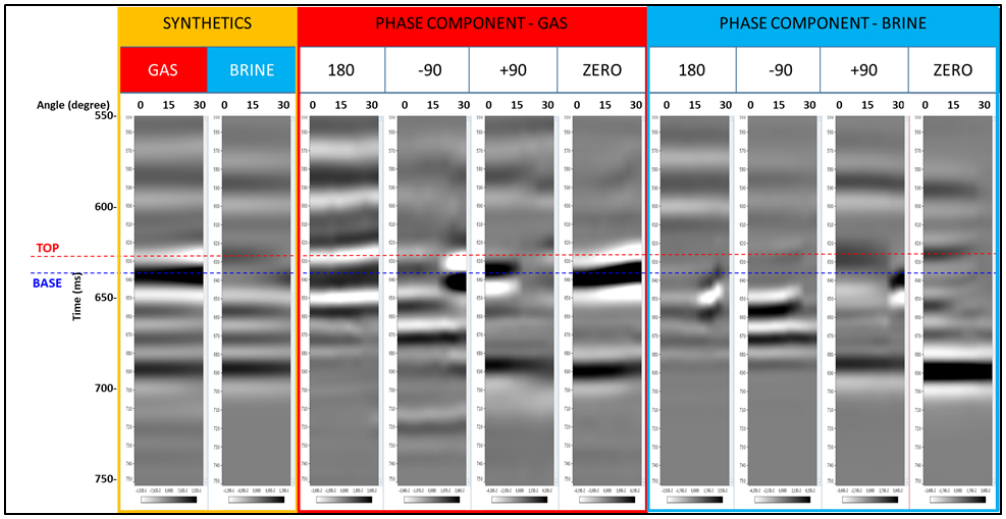

Figure 12: Phase components for fluid-substituted pre-stack synthetics calculated from the well logs. The two panels in the left (yellow highlighted) show the synthetic data for the gas and brine saturated cases. The following 4 panels in the center (red highlighted) show the phase components for the gas saturated case; and the last 4 panels in the right (blue highlighted) show the phase components for the brine saturated case. The phase components displayed are labeled at the top of each track.

82x42mm (300 x 300 DPI)

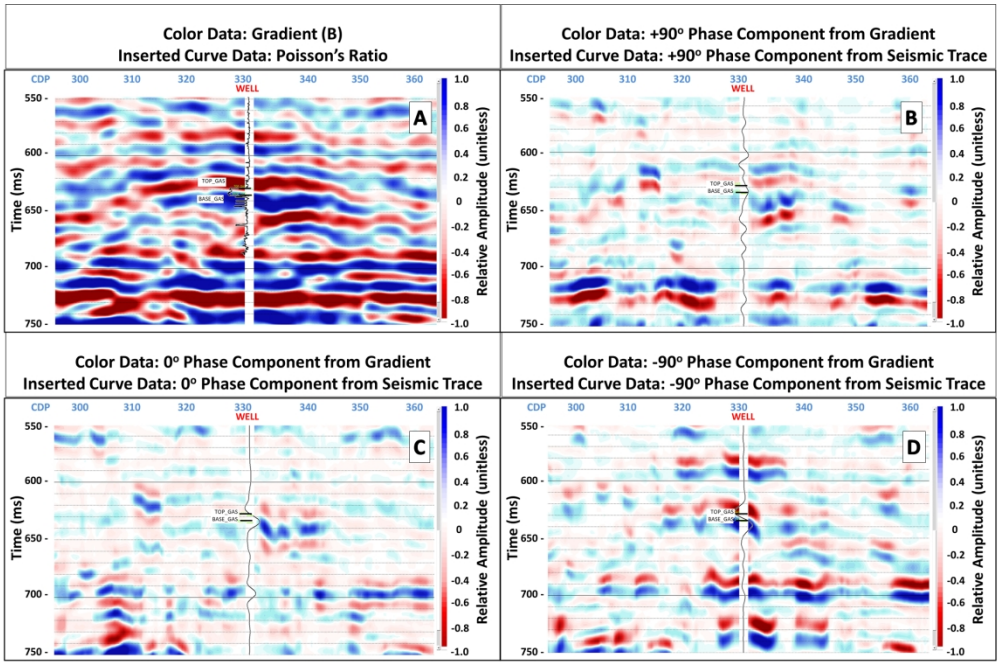

Figure 13: Phase component of the gradient calculated from seismic data. a): gradient with the Poisson's ratio log calculated from the well logs inserted at the well position,b) +90° component, c) 0° component, d) -90° component. The inserted trace for each panel is the phase decomposed synthetic trace from the well for the corresponding phase component displayed in the vertical section at the well position.

199x131mm (300 x 300 DPI)

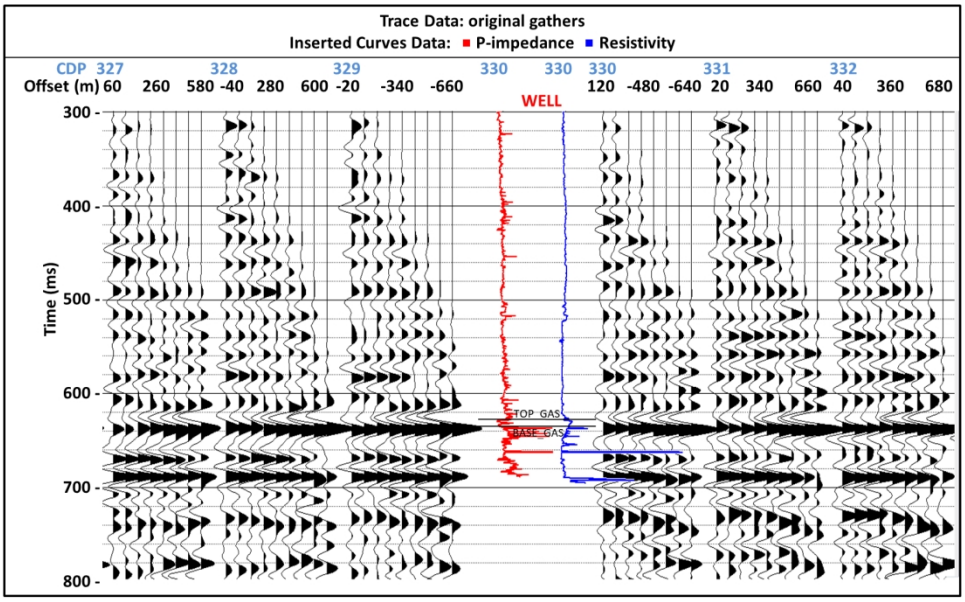

Figure 14: Original gathers at the well location (CDP 330) displaying the P-impedance (red curve) and resistivity (red curve) logs.

155x92mm (300 x 300 DPI)

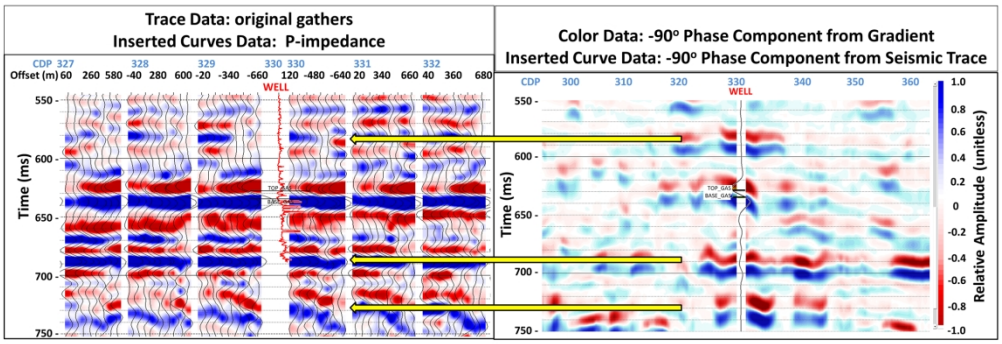

Figure 15: Comparison between the original gathers at the well location and the -90º phase component from the gradient attribute. The yellow arrows point to the loss of data quality at the far offsets for these events, resulting in anomalous -90° phase component from gradient.

196x67mm (300 x 300 DPI)